Journal of
Materials Chemistry C

PAPER

View Article Online
View Journal | View Issue

Published on 28 September 2015. Downloaded by Michigan State University on 19/01/2016 19:39:28.

Cite this: J. Mater. Chem. C, 2015, 3, 11239

Received 10th July 2015,
Accepted 24th September 2015

DOI: 10.1039/c5tc02090e

www.rsc.org/MaterialsC

$Zn_{1-x}Fe_xO$ films: from transparent Fe-diluted ZnO wurtzite to magnetic Zn-diluted Fe_3O_4 spinel

J. Perrière,[ab] C. Hebert,[ab] M. Nistor,*[c] E. Millon,[d] J. J. Ganem[ab] and N. Jedrecy*[ab]

The different phases formed in $Zn_{1-x}Fe_xO$ thin films where x varies from 0 to 1, as well as their structural characteristics and physical properties, have been investigated. In particular, the interrelationships between the iron concentration, the oxygen composition and the microstructure of the films have been determined. The $Zn_{1-x}Fe_xO$ films were grown on c-cut sapphire substrates by pulsed-laser deposition. For $0 < x < 0.35$, epitaxial films with a wurtzite (ZnO like) structure were obtained, while for $0.65 < x < 1$, spinel (Fe_3O_4 like) epitaxial films were observed. In the intermediate region ($0.35 < x < 0.65$) the phase separation of the $Zn_{1-x}Fe_xO$ films leads to the formation of both wurtzite and spinel phases. Whatever is the x value, the films display well-defined in-plane epitaxial relationships between the wurtzite (or spinel) phase and the substrate. The optical, electrical and magnetic properties of the $Zn_{1-x}Fe_xO$ films are discussed in relation with their structural characteristics.

Introduction

Following theoretical calculations,[1] transition metal doped ZnO was predicted as a promising diluted magnetic semiconductor with potential applications in spintronics. As a result, lot of effort has been devoted to the study of the growth and properties of ZnO thin films doped with various elements, whether magnetic or not.[2,3] However, the origin of ferromagnetism in such systems was claimed either an intrinsic property of doped ZnO, or due to the presence of a secondary metallic phase.[4,5] Moreover, observation of room temperature (RT) ferromagnetism in undoped ZnO films revealed that the transition metal may not play an essential role in introducing magnetism in ZnO.[6] In the case of Fe-doped ZnO,[7,8] the results are controversial and confusing, with papers reporting intrinsic ferromagnetism at RT or not, while others showing the co-existence of paramagnetic, anti-ferromagnetism and ferromagnetism contributions.[9] In addition, the presence or absence of Fe clusters has not been clearly established, except for a specific growth method, *i.e.* ion implantation followed by thermal annealing.[5,10]

To clarify the situation in the Fe-doped ZnO system, we have studied the phase diagram of $Zn_{1-x}Fe_xO$ films ($0 < x < 1$) by determining the nature of the phases present in the films and their physical properties. The $Zn_{1-x}Fe_xO$ films were grown by pulsed-laser deposition (PLD), which allows the control of oxygen incorporation in the films,[11] *i.e.* of the oxygen composition. The influence of the cationic ratio x = Fe/(Zn + Fe) on the structural characteristics has been determined, and the specific effects of the oxygen stoichiometry on the phase formation have been highlighted. The extreme values of x correspond to oxide materials presenting very different properties. The $x = 0$ value corresponds to the ZnO wide band gap oxide, a transparent conducting oxide (TCO), while $x = 1$ corresponds to magnetite Fe_3O_4, a ferromagnetic material with a high Curie temperature (858 K) presenting a half metallic behaviour. The optical, electrical and magnetic properties of the $Zn_{1-x}Fe_xO$ films were studied in view of establishing close correlations between the composition, structure and microstructure characteristics of the films with their physical properties.

Experimental

The zinc–iron oxide films were grown on c-cut sapphire by PLD, using a frequency quadrupled Nd:YAG laser (λ = 266 nm) delivering pulses (10 ns, 100 mJ cm^{-2}) irradiating the target.[12] The Zn–Fe-oxide ceramic targets were prepared by mixing powders of the precursor ZnO and Fe_2O_3 oxides to obtain the desired Zn/Fe proportion, followed by a sintering treatment at 1000 °C. Film growth was carried out at 500 °C under controlled pressure, between residual vacuum (5×10^{-7} mbar) up to 10^{-2} mbar oxygen pressure. After the growth the films were cooled down to room temperature (RT) at the oxygen pressure used during film deposition.

The film thickness and chemical composition were quantitatively determined by Rutherford backscattering spectrometry

[a] Sorbonne Universités, UPMC Univ. Paris 06, UMR 7588, INSP, F-75005, Paris, France. E-mail: nathalie.jedrecy@insp.jussieu.fr
[b] CNRS, UMR 7588, INSP, F-75005, Paris, France
[c] National Institute for Lasers, Plasma and Radiation Physics (NILPRP), L22 P.O. Box MG-36, 77125 Bucharest-Magurele, Romania. E-mail: mnistor@infim.ro
[d] GREMI, UMR 7344 CNRS-Université d'Orléans, F-45067 Orléans Cedex 2, France

Published on 28 September 2015. Downloaded by Michigan State University on 19/01/2016 19:39:28.

(RBS) using a 2 MeV ^{4}He ion beam. The MeV ion backscattering analysis provides the ability to distinguish the atomic masses of elements and their in-depth distribution as a function of the energy of the backscattered ions. The concentration profile of the various elements can be obtained from the simulation of the RBS spectra by the use of the RUMP program. A typical example of a $Zn_{1-x}Fe_xO$ film in the high x range may be found in ref. 13. The RBS measurements lead to 1% accuracy of the Zn and Fe concentrations. In contrast, owing to the low RBS yield on light elements, the oxygen content is only obtained with a 4% precision. The nature of the crystalline phases present in the films was studied by X-ray diffraction (XRD) using an X'Pert Panalytical 4 circles diffractometer with Cu K_α radiation. The film texture and epitaxial relationships with the substrates were also investigated.

The optical transmittance of the films was measured using a spectrophotometer Cary 5000 in the 190–3200 nm wavelength range. The electrical properties (resistivity as a function of temperature from liquid helium up to 300 K) were obtained by the classical four-probe method. The nature, concentration and mobility of charges were determined using a MMR Hall measurement system (in the van der Pauw geometry) at RT and under a magnetic field of 0.3 T. The magnetic properties of the films were measured by means of a vibrating sample magnetometer (VSM).

Results

Phase identification

The RBS measurements show that dense and smooth $Zn_{1-x}Fe_xO$ films in the 50–200 nm thickness range are obtained irrespective of the precise x value or the growth conditions used in this work. The iron atoms are uniformly distributed in the films, without noticeable segregation at the film/substrate interface or at the surface. The RBS analysis also shows that the films grown at the residual pressure (5×10^{-7} mbar) present a noticeable oxygen deficiency for $x \leq 0.05$, *i.e.* around 10% of oxygen atoms are missing with respect to the "parent" ZnO phase, the film composition being $Zn_{1-x}Fe_xO_{1-\delta}$ where $\delta \approx 0.1$. On the contrary, for $0.25 \leq x < 0.5$, the film composition is close to a stoichiometric compound $Zn_{1-x}Fe_xO_{1-\delta}$, where $-0.05 \leq \delta \leq 0.05$. Finally, for $x \geq 0.5$, the chemical composition is $Zn_{1-x}Fe_xO_{1+\delta}$ where $0.25 \leq \delta \leq 0.35$. In the latter case, the "parent" phase is Fe_3O_4 and the chemical composition of the film should be viewed as derived from the spinel $Zn_yFe_{3-y}O_{4-\beta}$ phase, where $y = 3 - 3x$ and $\beta = 1 - 3\delta$ accounts for the oxygen deficiency. For the sake of simplicity, the two types of phases (wurtzite and spinel) will be referred to in the rest of the paper using the generic term $Zn_{1-x}Fe_xO$ with $0 < x < 1$.

Fig. 1 represents θ–2θ XRD diagrams corresponding to $Zn_{1-x}Fe_xO$ films ($0 < x < 1$) grown on sapphire substrates under residual pressure (5×10^{-7} mbar), for 2θ values ranging between 28 and 40°, *i.e.* in the angular range where the main diffraction peaks of the two oxide compounds (ZnO wurtzite and Fe_3O_4 spinel) are present as indicated in the figure. These θ–2θ diagrams are normalized to the film thickness, and the peak intensity can thus be directly compared and used to evaluate the crystalline quality of the films.

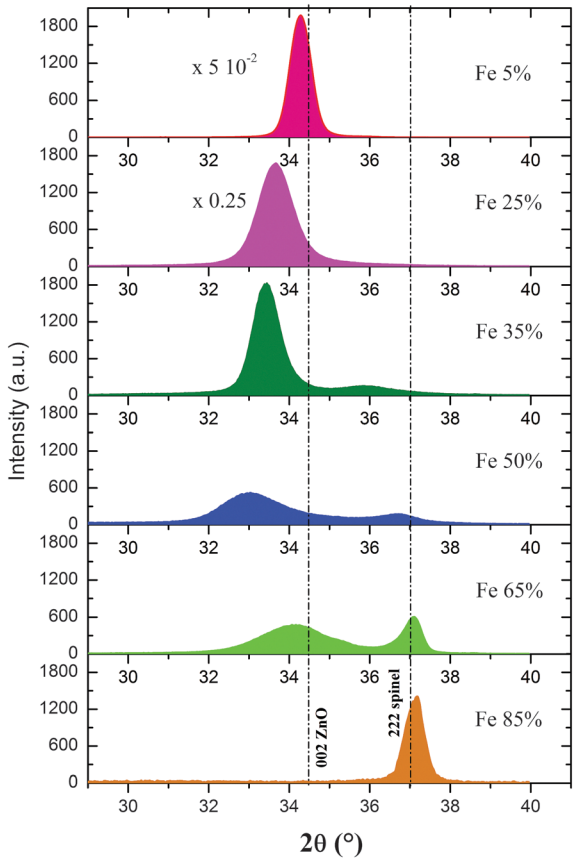

Fig. 1 θ–2θ diffraction patterns of films with different Fe concentration in the 2θ range 30–40°.

Schematically three domains in composition can be defined:

– At low x values ($0 < x < 0.35$), a sole peak is present corresponding to the 002 reflection of the hexagonal ZnO wurtzite structure, meaning that the Fe doped ZnO films present a (001) texture as observed for pure ZnO films grown under the same conditions. This peak is shifted towards decreasing 2θ values as x increases, indicating that the c lattice parameter of the wurtzite phase increases. Moreover, the overall peak area in the diagram largely decreases as x increases, indicating that the amount of the amorphous fraction of the film increases with the increasing Fe content.

– For the highest Fe concentrations ($x > 0.65$), a single peak located at about 37° is observed. It corresponds to the 222 reflection of the cubic zinc ferrite ($Zn_yFe_{3-y}O_4$) spinel structure, and both its position and width do not widely change with the x value. This is related to the fact that the lattice parameter value of the cubic zinc ferrite $Zn_yFe_{3-y}O_4$ shows a limited variation range between 8.395 Å ($y = 0$) and 8.43 Å ($y = 1$). At this stage, the discrimination between the different possible spinel phases ($Zn_yFe_{3-y}O_4$ or both Fe_3O_4, $ZnFe_2O_4$,) is not possible.

– In the intermediate region ($0.35 \leq x \leq 0.65$), the formation of both the wurtzite phase and a second oxide phase occurs *via* some kind of "phase separation" in the $Zn_{1-x}Fe_xO$ films.

 This journal is © The Royal Society of Chemistry 2015

Published on 28 September 2015. Downloaded by Michigan State University on 19/01/2016 19:39:28.

Indeed, for x = 0.35 a small peak appears at around 36°. Its position could correspond to the 111 reflection of the cubic FeO structure (a = 0.43 nm), indicating the presence of such FeO clusters in the ZnO wurtzite matrix. It has to be noticed that owing to the face centered cubic FeO structure, the 111 reflection should not be observed. However, the presence of defects related to oxygen deficiency and Zn incorporation in FeO would make the presence of the 111 peak possible in the θ–2θ diagram. Anyway, this peak disappears with the increasing x value (x = 0.5), while a well-defined 222 spinel peak is present at 36.9°. At this step, both wurtzite and spinel phases are textured on the c-cut sapphire substrate.

The c-axis parameter of the hexagonal wurtzite phase and the a-axis parameter of the cubic spinel phase were determined from the 002 ZnO and 222 spinel diffraction peaks in the θ–2θ diagrams, respectively. The a-axis parameter of the wurtzite phase was determined through the position of the 101 or 103 diffraction peaks. Fig. 2 summarizes these measurements and shows that the wurtzite c-axis is an increasing function of the Fe dopant concentration up to x = 0.5 for films grown under 5×10^{-7} mbar. On the other hand, the a-axis parameter does not show such large variations. These results evidence an expansion of the ZnO lattice along the c-axis as the Fe dopant concentration increases, which indicates that an increasing amount of Fe atoms is incorporated in the ZnO network. For x = 0.65, both wurtzite and spinel phases are present and the c-axis decreases, reaching a value similar to that observed for x = 0.05, indicating that the main fraction of Fe atoms is in the spinel phase.

Despite the incorporation of Fe in the wurtzite ZnO matrix, and the large variation in the c-axis parameter, the epitaxial growth of $Zn_{1-x}Fe_xO$ films on c-cut sapphire substrates was observed and investigated by pole figure measurements. Fig. 3 represents typical pole figures recorded for films grown in the wurtzite and spinel domains, respectively. For low x values (x = 0.25), *i.e.* wurtzite films, Fig. 3a shows the pole figure for the 101 ZnO reflection at 2θ = 36.25°, with 6 poles located at a declination angle Ψ = 61°. The azimuthal position of these poles allows deducing the following epitaxial relationship with the c-cut sapphire substrate:

$$Zn_{1-x}Fe_xO[100]//Al_2O_3[210] \quad \text{(I)}$$

This relationship corresponds to a 30° rotation of the hexagons of the (001) wurtzite plane with respect to the hexagons of the (001) Al_2O_3 plane. This is the classical epitaxial relationship observed for pure ZnO films grown on the c-cut sapphire substrate at 500 °C.[14] In this situation, the hexagonal close-packed oxygen sub-lattices in both the sapphire substrate and zinc oxide films may match together ensuring a continuity of the oxygen network through the film/substrate interface. For a large value of Fe concentration (x = 0.85), the spinel zinc ferrite phase is formed and epitaxial films were also observed as it can be deduced from Fig. 3b which represents the pole figure recorded for the 220 spinel reflection at 2θ = 29.8°. Six poles are observed on this figure at Ψ = 35°, *i.e.* the value expected for

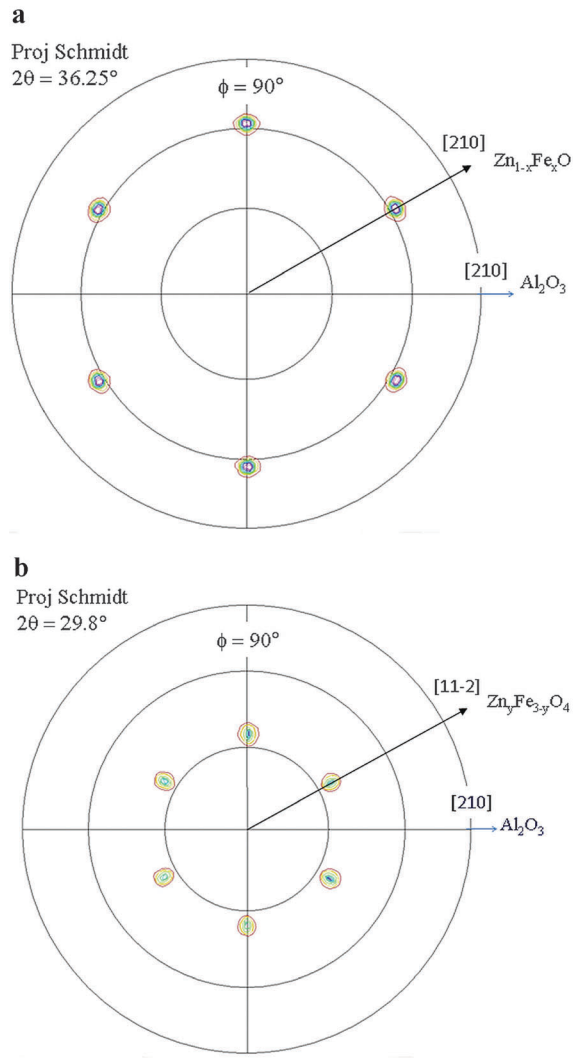

Fig. 3 Pole figures recorded for films (a) with x = 0.25 (wurtzite phase), and the (101) reflection (2θ = 36.25°); (b) with x = 0.85 (spinel phase), and the (220) reflection (2θ = 29.8°).

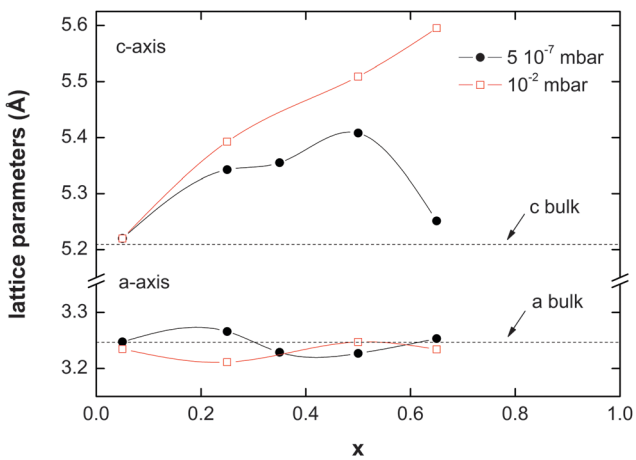

Fig. 2 Values of the lattice parameters of the wurtzite phase (c-axis and a-axis) as a function of the Fe concentration in films grown at 500 °C under 5×10^{-7} and 10^{-2} mbar.

Published on 28 September 2015. Downloaded by Michigan State University on 19/01/2016 19:39:28.

spinel crystallites with the (111) texture. The following in-plane epitaxial texture was deduced:

$$Zn_yFe_{3-y}O_4[10-1]//Al_2O_3[210] \quad \text{(II)}$$

This relationship also corresponds to a 30° rotation of the hexagons of the (111) spinel plane with respect to the hexagons of the c-cut sapphire substrate. In the intermediate domain ($0.35 < x < 0.65$), although a large fraction of the films is amorphous, both wurtzite and spinel phases are present and both are found to be epitaxially grown on the c-cut sapphire substrate.

For $0 < x < 0.65$, the wurtzite phase presents the epitaxial relationships of pure ZnO on the c-cut sapphire substrate grown under the same conditions, *i.e.* the classical 30° rotation of the film hexagons with respect to the sapphire hexagon substrate.[14] This epitaxial growth explains the absence of large variations of the *a*-axis parameter of the wurtzite phase (while the *c*-axis parameter shows noticeable variations). Indeed, a well-defined in-plane epitaxial relationship exists which is explained in the frame of the domain matching epitaxy.[15] The *a*-axis of the Fe doped ZnO phase is thus fixed by this epitaxial relationship and does not widely change with the increasing Fe concentration. On the contrary, the *c*-axis is not fixed by the in-plane epitaxial relationship and this leads to the expansion of the Fe doped ZnO crystallites along the *c*-axis.

Phase formation

The oxygen pressure during the growth was found to play an important role in the phase separation in the $Zn_{1-x}Fe_xO$ films. Fig. 4 compares the θ–2θ XRD diagrams of $Zn_{0.5}Fe_{0.5}O$ films grown at the residual pressure and 10^{-2} mbar, respectively. For the films grown at low pressure the 222 reflection of the zinc ferrite spinel phase is observed, while at high pressure (10^{-2} mbar), this peak is not present. Moreover the 002 wurtzite peak is more shifted towards the lowest 2θ values at 10^{-2} mbar than at residual pressure, indicating a higher *c*-axis value and thus a higher concentration of Fe in the wurtzite phase. In the same way its intensity is lower than that at residual pressure meaning that the amorphous fraction of the film is higher at 10^{-2} mbar. The films grown under 10^{-2} mbar oxygen pressure also show that the *c*-axis is an increasing function of the Fe concentration up to $x = 0.65$, from which the phase separation into wurtzite and spinel phases occurs (Fig. 2). All these points mean that the phase separation of $Zn_{1-x}Fe_xO$ films into wurtzite and spinel phases is favored under low oxygen pressure growth, *i.e.* under conditions where oxygen deficient films are formed. These results are in agreement with previous results on the phase separation, which occurs in oxygen deficient tin doped indium oxide which can lead, for a complete phase separation, to the formation of metallic clusters in a stoichiometric matrix.[16–18] It has to be noticed that diffraction peaks associated with Fe metal clusters were never observed in this work even for high Fe concentrations.

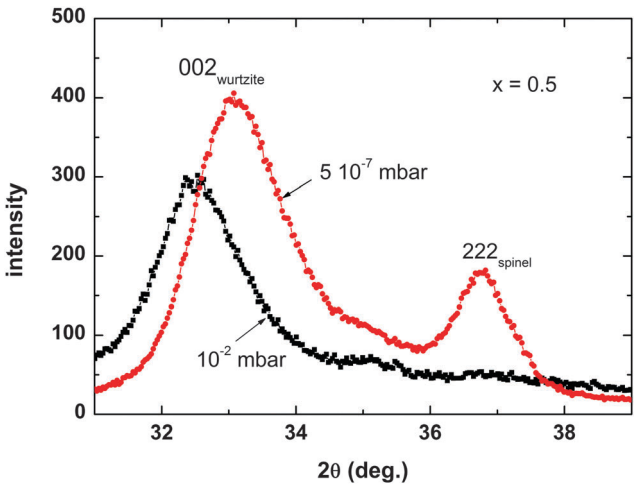

Fig. 4 θ–2θ diffraction patterns of films ($x = 0.5$) grown under 5×10^{-7} mbar and 10^{-2} mbar oxygen pressure.

The appearance of a secondary phase (FeO and/or spinel) in the θ–2θ XRD diagrams *via* the phase separation in $Zn_{1-x}Fe_xO$ films occurs for $x \geq 0.35$ under residual pressure conditions. Such a concentration is largely higher than the solubility limit of Fe in ZnO which is in the 1.5–5% range following previous reports.[19,20] It has been shown in the case of nanoparticles assembly that the overall Fe solubility in ZnO drastically increases with the decreasing size of the ZnO nanoparticles. Indeed the overall solubility of Fe in nanograined ZnO films (grain size is 6–15 nm, determined by XRD and TEM measurements) reaches about 20 at% at 550 °C.[21] The reason would be the accumulation of Fe towards the external zone of the nanoparticles leading to the formation of Fe-enriched ZnO amorphous boundaries with a thickness up to 1 nm.[21] The Fe rich amorphous boundaries are supposed to be at the origin of the secondary phase which appears at increasing Fe concentrations. Such a segregation of transition metal at the grain boundaries in $Zn_{1-x}Mn_xO$ films has also been inferred from electron paramagnetic resonance and transmission electron microscopy analyses.[22]

The comparison with the results reported here leads to the conclusion that a similar phenomenon occurs during the $Zn_{1-x}Fe_xO$ film growth at 500 °C under 5×10^{-7} mbar. Actually, in addition to the shift of the ZnO-like 002 peak, broadening of this peak is observed with the increase in Fe concentration (Fig. 1). The width of the 002 peak depends upon both the crystallite size (coherent domain) and microstrain in the film. To precisely determine the grain size, the Williamson–Hall plot should be used, but in the case of textured (00*l*) ZnO films such an approach leads to inaccurate values. For comparison, we have thus only used the Debye–Scherrer formulae to estimate the grain size of the ZnO crystallites in our films. This estimation through the Debye–Scherrer formulae leads to values ranging from 16 nm for $x = 0.05$ to 10 nm for $x = 0.35$, a variation similar to that reported in the case of granular films.[21] At the same time, Fig. 1 shows that the intensity of the 002 peak largely decreases, indicating a decrease of the ZnO crystalline phase present in the films, *i.e.* amorphous regions are created with the increase in Fe concentration. The decrease in the ZnO grain size and the decrease of the amount of crystalline ZnO

 This journal is © The Royal Society of Chemistry 2015

Published on 28 September 2015. Downloaded by Michigan State University on 19/01/2016 19:39:28.

can thus be explained by the formation of Fe rich amorphous grain boundaries (and later the formation of crystallized FeO-like grains).

Electrical properties

The Hall measurements indicate that n-type films are formed irrespective of the Fe concentration. In oxide films, the oxygen stoichiometry plays an important role in the resistivity since oxygen vacancies usually act as electron donors. Depending upon the oxygen pressure during the PLD growth, the resistivity of the $Zn_{1-x}Fe_xO$ films presents very large variations. In what follows, we only present the results concerning the films grown at a residual pressure of 5×10^{-7} mbar. Fig. 5 shows the resistivity as a function of the Fe concentration. The density and mobility of the carriers deduced from the Hall measurements are given for $0 < x < 0.4$ for which no magnetic phase is present, thus avoiding the existence of the anomalous Hall effect.

For $0 \leq x \leq 0.35$, the resistivity ρ drastically increases with Fe concentration. Indeed, while at $x = 0.05$, ρ is close to the value measured for pure ZnO films grown under the same conditions (about 10^{-2} Ω cm), for $x = 0.25$ the ρ value is 4×10^3 times higher. This large increase is due to a decrease of both the density and mobility of carriers as shown in Fig. 5, and it has to be related to the microstructural characteristics of these films. Actually with an increase in Fe concentration, the size of the ZnO crystallites decreases and Fe rich amorphous grain boundaries are formed. Scattering of the electrons in these grain boundaries are presumably very important and drastically reduces the carrier mobility. The decrease in the carrier density could be related to the presence of both Fe^{3+} and Fe^{2+} in the wurtzite phase.[7,23] In fact, the carrier density in ZnO films is related to the presence of oxygen vacancies. The decrease of the carrier density means neutralization of these oxygen vacancies and this can be obtained by the transformation of Fe^{3+} cations into Fe^{2+} cations. These changes lead to the annihilation of oxygen vacancies, and the increase in Fe concentration will thus drastically decrease the carrier density. It has to be noticed that the change from Fe^{3+} to Fe^{2+} would lead to modifications in the wurtzite lattice. In fact, the Fe^{3+} ionic radius (0.64 Å) is lower than that of Zn^{2+} (0.74 Å), and thus does not lead to an expansion of the ZnO lattice. Differently, the presence of Fe^{2+} (ionic radius equal to 0.76 Å) will induce an expansion of the ZnO network. The increase in Fe^{2+} amount in the ZnO network with the increasing Fe concentration would, at least partly, explain the large expansion of the ZnO unit cell along the *c*-axis (see Fig. 1 and 2).

In the spinel domain ($0.65 < x < 1$), the carrier transport occurs in the zinc ferrite phase (which is the sole phase present in this domain) with a low resistivity of $2–4 \times 10^{-2}$ Ω cm, which is similar to that measured in $Zn_yFe_{3-y}O_{4-\delta}$ (y = 0.3–0.9) thin films grown under reducing conditions.[13,24]

A maximum of resistivity is observed for $x = 0.35$, *i.e.* just at the beginning of the phase separation in which FeO or/and spinel crystallites start to form. Then in the intermediate wurtzite and spinel domain ($0.35 \leq x \leq 0.65$) the resistivity is a decreasing function of the Fe concentration. This resistivity variation in this domain is characteristic of the presence of both highly defective and resistive Fe doped ZnO nanograins, and crystalline spinel presenting a noticeable conductivity. The increase in the Fe concentration increases the amount of the spinel phase at the expense of the Fe doped ZnO, and as a result the overall resistivity decreases.

To obtain more information on the carrier transport, the resistivity as a function of temperature ($\rho(T)$ curve) was measured, and Fig. 6 shows the main results. All the curves present a negative temperature coefficient of resistivity (TCR), *i.e.* an increase in resistivity with decreasing temperature, but this common behaviour does not mean that all the films are classical semiconductors. Actually, for $x = 0.05$, the ratio of the resistivity at 5 and 300 K ($\rho(5)/\rho(300)$) is about 1.3, while it is largely higher than 10 for the other curves. This 1.3 value is not expected for a classical semiconductor presenting a thermally activated transport mechanism. The carrier density in these films (1.3×10^{19} cm^{-3}) being higher than the critical Mott

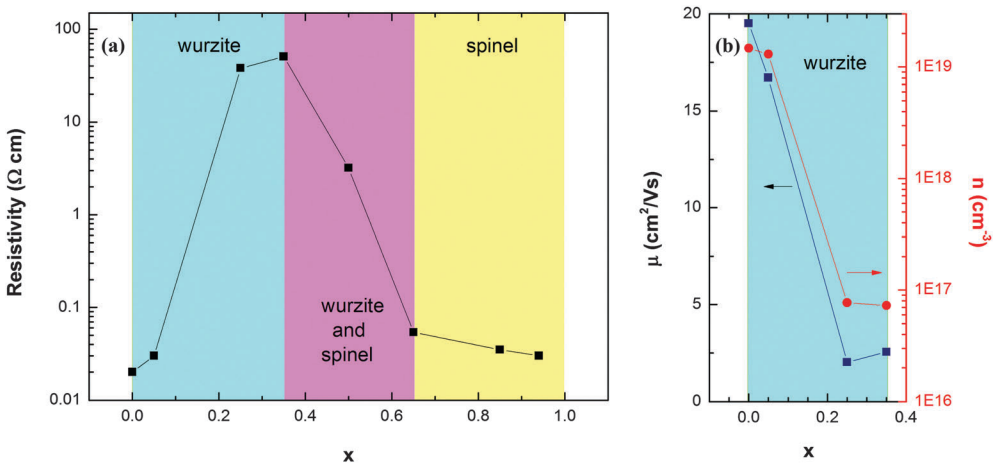

Fig. 5 (a) Resistivity ρ as a function of the Fe concentration for films grown under 5×10^{-7} mbar at 500 °C; (b) density and mobility of the carriers in the $0 < x < 0.35$ concentration range.

Published on 28 September 2015. Downloaded by Michigan State University on 19/01/2016 19:39:28.

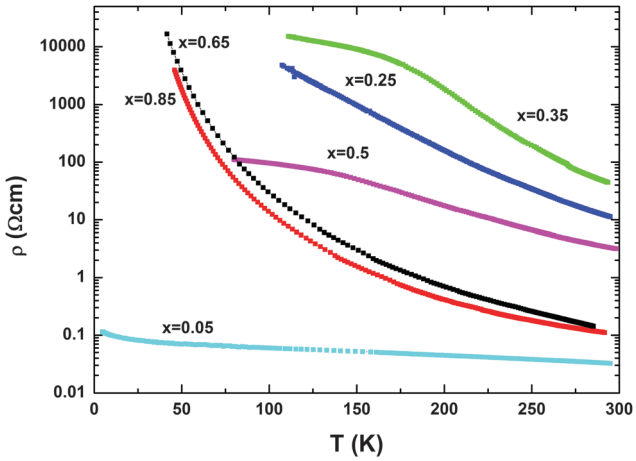

Fig. 6 Temperature dependant resistivity (ρ) for films with different x values.

density for ZnO, *i.e.* from 5×10^{18} to 1×10^{19} cm^{-3} following the reports,[25,26] these films are degenerated, and a metallic behaviour should be observed in the $\rho(T)$ curve. However, 5% Fe doping induces a structural disorder in the films, and the defects act as scattering centres for the carriers. This leads to an increase of the resistivity. The negative TCR in Fig. 6 for the 5% Fe doped films can thus be observed when the Fermi wavelength λ_F(*i.e.* $2\pi/(3\pi^2 n)^{1/3}$) becomes comparable to the electronic mean free path L(*i.e.* $h/\rho n e^2 \lambda_F$) due to large scattering of the carriers.[27,28] These two values are of the same order for these films, 3.2 and 1.25 nm respectively. Under these conditions, the negative TCR and small increase in resistivity with decreasing temperature are due to the quantum corrections to conductivity.[27] Such a behaviour has already been observed in disordered pure or doped ZnO and other oxide films.[28,29]

The other $\rho(T)$ curves in Fig. 6 present a more classical semiconductor behaviour, with a negative TCR leading to a large increase of resistivity with decreasing temperatures. This is mainly due to a lower carrier density in the films (see Fig. 5), excluding thus the formation of degenerate semiconductors. Such curves are generally explained in the high temperature part, by a thermally activated transport mechanism described by the following equation:

$$\rho(T) = \rho_0 \exp(E_0/kT)$$

where E_0 is the activation energy for the transport. Then with decreasing temperature, the thermal energy is no longer sufficient to move electrons in the conduction band, and localisation of the carriers occurs. The thermally activated regime is then followed at lower temperatures by the variable range hopping (VRH) mechanism proposed by Mott in which the resistivity is described by the following relationship:

$$\rho(T) = \rho_{M0} \exp(T_{M0}/T)^{1/4}$$

The charge transport occurs by hopping from a localized site to another site in the vicinity of the Fermi level.[30] A development of this model has been proposed by Efros–Shklovskii (ES),[31] which takes into account the Coulomb interaction between localized carriers. This leads to the following temperature variation for the resistivity:

$$\rho(T) = \rho_{ES0} \exp(T_{ES0}/T)^{1/2}$$

In these relationships, T_{M0} and T_{ES0} are the characteristic temperature of each VRH model.

Fig. 7a and b present the curves resulting from this analysis for three typical cases. For $x = 0.85$, the film is solely composed of the spinel phase, and the Arrhenius plot $\ln \rho = f(1/T)$ in Fig. 7a shows a linear part between RT and about 120 K. The activation energy E_0 deduced from the slope is equal to 68 meV, a value close to those reported for zinc ferrite films.[13,20] For $T <$ 120 K, the Arrhenius plot is no longer linear and the Mott VRH approach is shown in Fig. 7b, with the $\ln \rho = f(1/T^{1/4})$ plot. A linear variation is observed for 120 K $< T <$ 80 K, leading to a T_{M0} value equal to 5.55×10^7 K, similar to those previously reported.[13] The inset in Fig. 7b presents the plot ($\ln \rho = f(1/T^{1/2})$) corresponding to the ES model, and shows a linear variation between 80 and 40 K, indicating that a crossover from the Mott VRH to the ES VRH model is observed in the pure spinel film, as been observed and modelled in the case of other oxide films.[32,33]

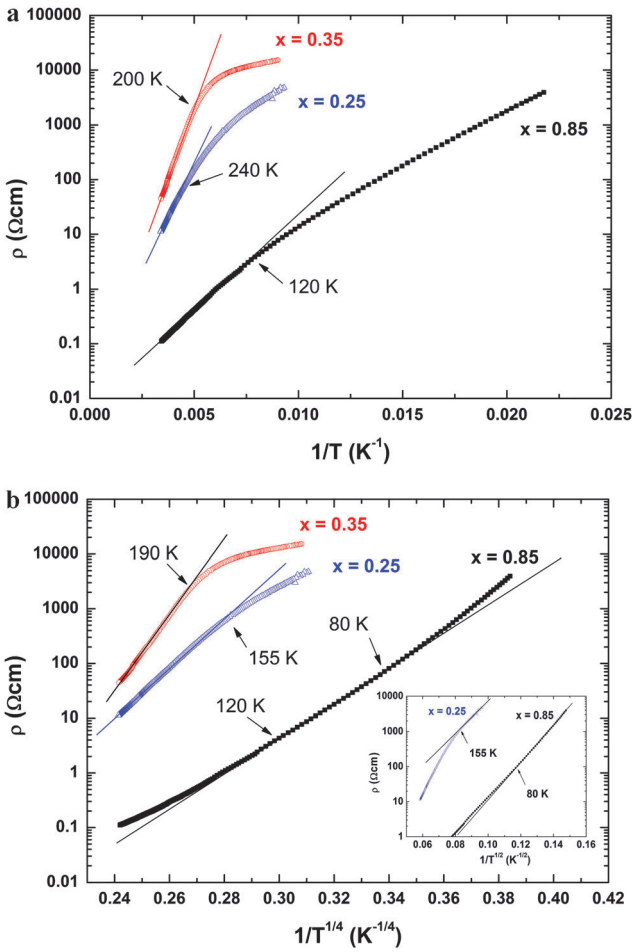

Fig. 7 (a) Variation of log(ρ) with (1/T) for films with various Fe concentrations; (b) variation of log(ρ) with (1/$T^{1/4}$) for films with various Fe concentrations; the inset shows the variation of log(ρ) with (1/$T^{1/2}$).

 This journal is © The Royal Society of Chemistry 2015

Published on 28 September 2015. Downloaded by Michigan State University on 19/01/2016 19:39:28.

Table 1 Electrical and optical parameters of various films with $0 < x < 1$ Fe concentrations (E_0 activation energy for the thermally activated transport mechanism, T_{M0} Mott temperature of variable range hopping (VRH) mechanism)

	E_0 (meV)	T_{M0} (K)	Direct band gap (eV)	Indirect band gap (eV)
$x = 0.05$	—	—	3.31	—
$x = 0.25$	—	1.34×10^8 (300–175 K)	3.37	—
$x = 0.35$	191 (300–200 K)	2.5×10^5 (150–50 K)	3.38	—
$x = 0.5$	95 (300–210 K)	1.6×10^7 (210–160 K)	—	—
$x = 0.65$	82 (300–130 K)	4.35×10^7 (110–50 K)	3.17	1.67
$x = 0.85$	68 (300–120 K)	5.55×10^7 (120–80 K)	2.79	1.54

Table 1 shows the values of E_0 and T_{M0} obtained for the various $Zn_{1-x}Fe_xO$ films. For the $Zn_{0.35}Fe_{0.65}O$ composition, the E_0 and T_{M0} values are rather close to those of the pure spinel ($x = 0.85$), in agreement with Fig. 6, which shows a very similar behaviour for the $\rho(T)$ curves of these two samples. This means that some kind of percolation occurs in the $Zn_{0.35}Fe_{0.65}O$ films, with a current passing through the zinc ferrite phase and avoiding the higher resistive wurtzite phase. The $\rho(T)$ curves of the two other films of the mixed region ($Zn_{0.65}Fe_{0.35}O$ and $Zn_{0.5}Fe_{0.5}O$) have been analysed by the same approach; however the physical meaning of the values (E_0 and T_{M0}) is less clear. Actually, both wurtzite and spinel phases are present and both contribute to the electronic transport but their respective contribution to the resistivity is not known, and cannot be extracted straightforwardly from the E_0 and T_{M0} values given in Table 1.

Finally, Table 1 shows that an E_0 value is not given for the $Zn_{0.75}Fe_{0.25}O$ film. In fact a very good fit was obtained using the Mott VRH model from RT down to 155 K (Fig. 7b), representing a far better fit than that obtained by the thermally activated transport mechanism in Fig. 7a (E_0 = 160 meV, from 300 to 250 K). This means that this film is in the strong localization regime at RT leading to the hopping transport mechanism. This has to be related to the very important disorder[25,29] in this film, due to the large incorporation of Fe (25%) in the ZnO wurtzite network. Below 155 K, the resistivity of this film varied with the Efros–Shklovskii (ES) model, as shown by the linear variation observed in Fig. 7b. In this case, a crossover from Mott VRH to ES VRH is also present.

Optical properties

Fig. 8a and b show the optical transmittance spectra in the UV-visible and near infrared domain (300–3200 nm) for $Zn_{1-x}Fe_xO$ films with different Fe concentrations. For the lowest x values ($x < 0.35$), the curves in Fig. 8a are similar to that recorded for a pure ZnO film grown under same conditions. Actually these curves present a high transmittance (>85%) in the visible and near infrared wavelength domain (500–3200 nm). On the contrary, for Fe concentrations corresponding to mixed ($Zn_{0.35}Fe_{0.65}O$) or spinel ($Zn_{0.15}Fe_{0.85}O$) films, a large decrease in the optical transmittance in the 500–3200 nm domain is clearly observed in Fig. 8b.

The optical band gap energy E_g of such oxide films was classically deduced from the absorption coefficient α using the Tauc relationship[34]

$$\alpha h\nu = A(h\nu - E_g)^q$$

where α is the optical absorption, $h\nu$ is the incident photon energy, A is a constant and q characterizes the optical

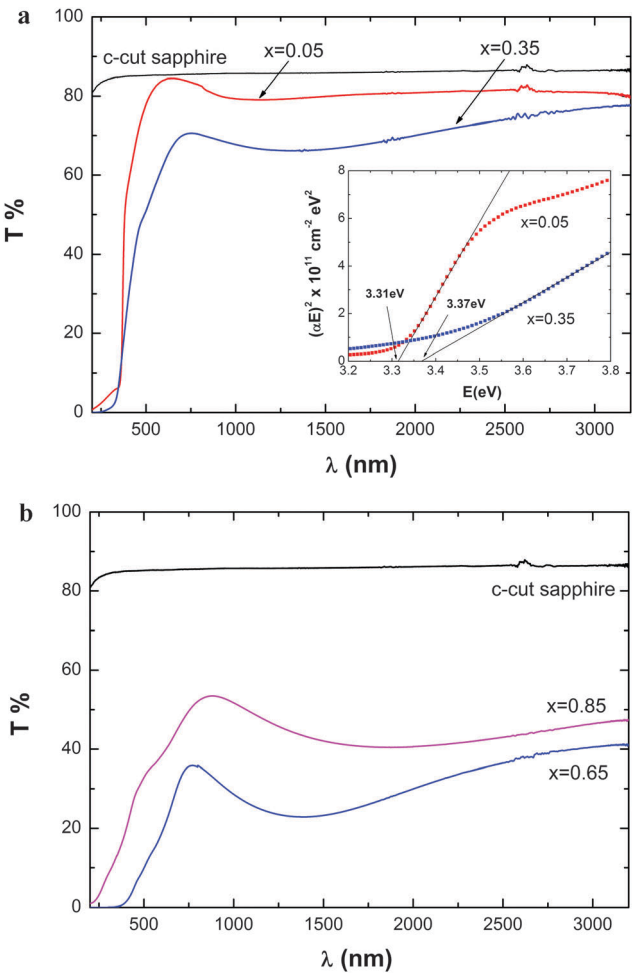

Fig. 8 UV-visible-near IR transmittance for (a) films with $x < 0.35$, the inset shows the corresponding Tauc plot; (b) for films with $x > 0.65$.

absorption process with a value equal to 2 or $\frac{1}{2}$ for allowed indirect and direct electronic transitions, respectively.[34] It follows that in a plot of $(\alpha h\nu)^{1/q} = f(h\nu)$, the extrapolation to $\alpha = 0$ of the linear portions of $(\alpha h\nu)^2$ and $(\alpha h\nu)^{1/2}$ plot would lead to the determination of the direct and indirect band gap values, respectively.[34]

In the inset of Fig. 8a, the Tauc plot corresponding to the wurtzite domain ($x < 0.35$) leads to the determination of the direct band gap E_g values, and are given in Table 1. For undoped ZnO films ($x = 0$) the optical bandgap depends upon the growth methods and conditions and is generally found to be around 3.3–3.4 eV. The values reported in Table 1 lie in this

Published on 28 September 2015. Downloaded by Michigan State University on 19/01/2016 19:39:28.

domain and show that for Fe concentrations in the 25–35% range, the E_g value (3.37–3.38 eV) is higher than that obtained for the 5% Fe concentration (3.31 eV), while generally the band gap value of Fe doped ZnO films is found to decrease with increasing Fe concentrations. It has to be noticed that the $Zn_{0.95}Fe_{0.05}O$ film presents a high carrier density (1.3×10^{19} cm^{-3}) which makes it degenerated, *i.e.* a band gap renormalization has occurred leading to the band gap shrinking which can explain the low E_g value for the $Zn_{0.95}Fe_{0.05}O$ film.

Fig. 9a and b show the $(\alpha h\nu)^2$ Tauc plot for the mixed and spinel domains, respectively. For the mixed domain ($x = 0.65$) a direct band gap value (3.17 eV) was deduced (Fig. 9a) which could be related to the presence of the Fe doped ZnO wurtzite phase, as this value is relatively close to the ZnO band gap. In the inset of Fig. 9a, the $(\alpha h\nu)^{1/2}$ Tauc plot leads to a value of 1.67 eV for the indirect band gap which has to be related to the zinc ferrite spinel phase. Actually indirect band gap values in the 1.5–1.7 eV range have been reported for this phase.[35–37] In Fig. 9b, the direct band gap value (2.79 eV) is close to the value reported for the zinc ferrite spinel phase[35–37] in agreement with the XRD results showing solely the presence of this phase. Moreover, a value equal to 1.54 eV is obtained from the $(\alpha h\nu)^{1/2}$ Tauc plot (indirect band gap) presented in the inset in Fig. 9b. The rather large scattering of the direct and indirect bandgap values may be related to the differences in the zinc ferrite composition and to the different growth conditions with respect to the previous reports.[35–37]

Magnetic properties

The magnetic measurements were carried out at 300 K for each type of sample by applying the magnetic field $\mu_0 H$ in the plane of the films. The magnetization evolution as a function of H is shown in Fig. 10a and b. For $x = 0.05$, a very faint magnetic signal is observed at the detection limit of the apparatus (Fig. 10a). From $x = 0.05$ up to $x = 0.35$, the magnetic signal gets more intense, and the magnetization value at saturation seems to increase linearly with x. However, the saturation magnetization value achieved at $x = 0.35$ is only 11 kA m^{-1}. Assuming 0.35 Fe atom per ZnO formula unit, the average magnetic moment per Fe atom is equal to 0.08 μ_B, where μ_B is the Bohr magneton. As we know from the X-ray results that a secondary phase exists at $x = 0.35$ with a composition close to FeO which is antiferromagnetic, this magnetic moment per Fe atom may be underestimated. In any case, its value remains

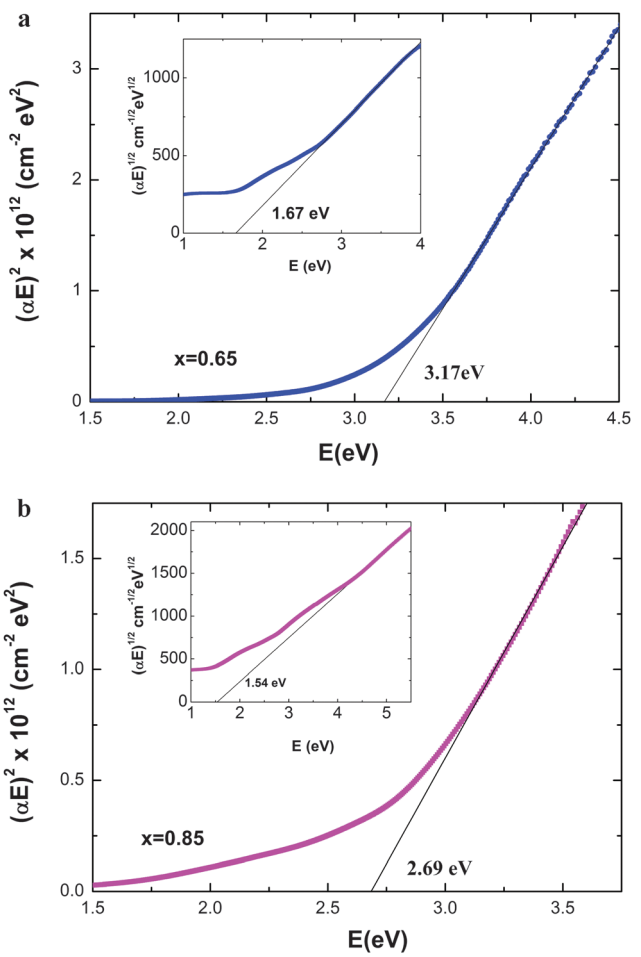

Fig. 9 Tauc plot for the direct band gap and the inset shows the tauc plot for the indirect bandgap for (a) the film with $x = 0.65$; (b) the film with $x = 0.85$.

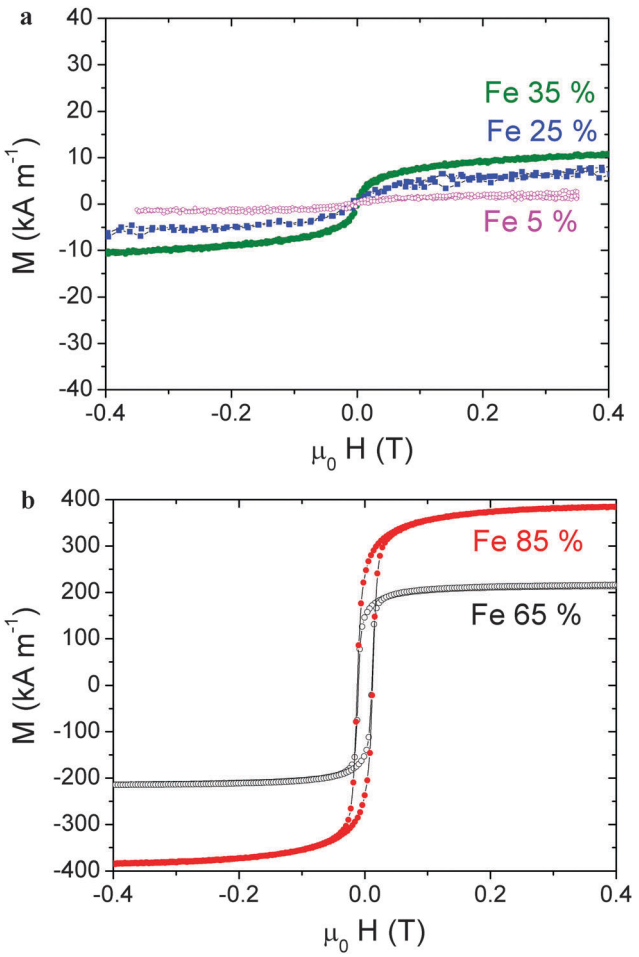

Fig. 10 M–H curves recorded at 300 K for (a) wurtzite type films ($x < 0.35$); (b) films with spinel and both spinel and wurtzite phases ($x > 0.65$).

 This journal is © The Royal Society of Chemistry 2015

Published on 28 September 2015. Downloaded by Michigan State University on 19/01/2016 19:39:28.

very low compared to the known magnetic moments carried by Fe^{2+} or Fe^{3+} cations in oxides, which are equal to 4 μ_B and 5 μ_B, respectively. Hence, whatever be the exact proportion of Fe^{2+} and/or Fe^{3+} cations in our films, their magnetic moments do not couple ferromagnetically. As a confirmation, no hysteresis is observed; the remanent magnetization M_r and the coercitive field H_c are equal to zero. Similar to the case of the Co-doped ZnO films which have been studied for a long time with controversy (for a review, see ref. 38), ferromagnetism is not observed in the Fe-doped ZnO films provided that the wurtzite phase does not coexist with a ferromagnetic secondary phase (*e.g.* metallic clusters).

Distinctly, a strong magnetization signal together with a $M(H)$ hysteresis cycle are observed for $x = 0.65$ (Fig. 10b). The value at saturation (M_s) is equal to 216 kA m^{-1}, the M_r remanent magnetization is 70% of M_s, and the coercitive field H_c is equal to 11 mT. For a direct comparison with the $x = 0.35$ case, under assumption of randomly dispersed Fe atoms in a ZnO matrix, the M_s value measured for $x = 0.65$ would correspond to 0.85 μ_B per Fe atom (with respect to 0.08 μ_B determined for $x = 0.35$). For $x = 0.85$, a $M(H)$ hysteresis cycle is also observed, with the saturation magnetization M_s reaching 384 kA m^{-1}, *i.e.* 1.16 μ_B per Fe atom. One may notice the coercitive field is the same as that for $x = 0.65$. For $0.65 \leq x \leq 0.85$, the room temperature ferromagnetic properties must be analyzed in the context of the spinel oxide phase, instead of the wurtzite phase. At $x = 0.85$, the spinel structure is solely detected in the X-ray diagram and the $Zn_{1-x}Fe_xO$ film consists of a $Zn_yFe_{3-y}O_{4-\beta}$ spinel oxide, with an oxygen deficient sublattice. In more detail, the $Zn_{0.15}Fe_{0.85}O_{1.2}$ film composition derived from the RBS analysis must be understood as $Zn_{0.45}Fe_{2.55}O_{3.6}$. In the parent magnetite Fe_3O_4 spinel, the magnetic moment per formula unit is 4 μ_B because of the antiferromagnetic coupling between the Fe^{3+} cations (5 μ_B) in the tetrahedral sites and the $Fe^{2+}//Fe^{3+}$ (4//5 μ_B) cations in the octahedral sites. This leads to 4/3 μ_B per Fe atom in a spinel matrix. As the Zn^{2+} cations substitute Fe^{3+} in the tetrahedral sites, the magnetic moment m_{Fe} per Fe atom in $Zn_yFe_{3-y}O_{4-\beta}$ is expected to be equal to $m_{Fe} = (4 + 6y - 2\beta)/(3 - y)$ μ_B. The $x = 0.85$ value corresponds to $y \approx 0.45$ (and $\beta = 0.4$), at which the magnetic moment per Fe atom is thus worth "on theory" 2.3 μ_B. The experimental value of 1.16 μ_B is 50% of the ideal value because (i) the Zn fraction in the spinel is herein high enough to disturb the AF coupling between the Fe magnetic moments in the octahedral and the tetrahedral sites, (ii) the measurement is carried out at 300 K (the magnetization is known to decrease with respect to increasing temperature according to the Bloch law), (iii) antiphase boundaries may reduce the overall magnetization of films. Nevertheless, the ferromagnetic signal is high and unambiguous. The zinc ferrite $Zn_yFe_{3-y}O_{4-\delta}$ spinel films and their magnetic properties have been recently studied in more detail in ref. 13. At $x = 0.65$, the ZnO wurtzite and the $Zn_yFe_{3-y}O_4$ spinel phases coexist (see Fig. 1). The intensity of the spinel peak in the X-ray diagram is about half that at $x = 0.85$. As a matter of fact, the magnetic signal for $x = 0.65$ is reduced by about two with respect to the signal for $x = 0.85$, while the magnetic characteristics of the hysteresis cycle (M_r/M_s and H_c) are unchanged. One may reasonably consider the film $x = 0.65$ as consisting of a mixture of non-magnetic wurtzite ZnO crystallites and room temperature ferromagnetic spinel $Zn_{0.45}Fe_{2.55}O_4$ crystallites in an almost equal proportion. Such a repartition of the wurtzite and spinel phases can explain the percolation phenomenon through the spinel phase which has been deduced from the measurements of transport properties (Fig. 6 and 7) in the $x = 0.65$ film.

Discussion

Depending upon the Fe concentration, Fe-diluted ZnO wurtzite and/or Zn-diluted Fe_3O_4 spinel phases were found in the $Zn_{1-x}F_xO$ films. Actually, for $x < 0.35$, epitaxial films with a wurtzite structure are formed, while for $x > 0.65$, spinel epitaxial films are observed. In the intermediate region ($0.35 < x < 0.65$), the films are constituted by both wurtzite and spinel phases.

The formation of such a mixture of phases is not so trivial as the chemical reactions leading to wurtzite ZnO and pure Fe spinel (Fe_30_4) or Fe–Zn spinel ($ZnFe_2O_4$) is linked to oxygen pressure and to the relative stability of each phase. For a given oxygen pressure the free energy of the oxide formation from one mole of O_2 is lower for ZnO (−640 kJ) than for Fe_3O_4 (−507 kJ) or $ZnFe_2O_4$ (−532 kJ),[39] meaning that the crystallisation of the ZnO phase will be the driving force during the growth of a $Zn_{1-x}Fe_xO$ based film. It comes out that the ZnO phase may grow at the expense of the remaining oxide film which will become more and more oxygen deficient, *i.e.* the Fe^{2+}-based oxide phase may therefore be preferentially formed after ZnO. This means that FeO (Fe^{2+} valence state) would be first preferentially synthesized with respect to Fe_3O_4 (mixed valence states Fe^{2+} and Fe^{3+} phase) or $ZnFe_2O_4$ (pure Fe^{3+} valence state).

Depending on the growth conditions, the phase separation can be partial (leading to the formation of a suboxide) or complete (metallic clusters can be formed in a stoichiometric oxide matrix) as previously observed.[15–17] In our work, diffraction peaks associated with Fe metal clusters were never observed. It means that a complete phase separation does not occur under our experimental growth conditions. This could be due to firstly, the residual pressure which is not sufficiently low to induce a sufficient oxygen deficiency in the film, and secondly, the fact that iron oxide phases with low energy formation exist. Actually Fe clusters in a ZnO matrix have been solely obtained by Fe ion implantation followed by an annealing treatment.[5,10] However, pre-annealing of the ZnO crystal under vacuum (*i.e.* under reducing conditions) before Fe implantation hindered the formation of Fe clusters, and preferentially led to the formation of the zinc ferrite phase.[5,40] The defects induced in the ZnO crystal by the reducing annealing (oxygen vacancies) seem to favor the formation of the zinc ferrite phase at the expense of the Fe metallic clusters.[5,40] In our work, comparable conditions are present in the oxygen deficient $Zn_{1-x}Fe_xO_{1-\delta}$ films, and the formation of the zinc ferrite phase occurs instead of the synthesis of Fe clusters in the ZnO matrix. It has to be noticed that while the pre-annealed

Published on 28 September 2015. Downloaded by Michigan State University on 19/01/2016 19:39:28.

ZnO crystal doped with Fe does not show metallic Fe cluster formation, such a treatment does not prevent Co cluster formation in similar experiments.[5] We have obtained the formation of metallic Co clusters in a ZnO matrix using PLD of a highly Co-doped (50%) ZnO target at 500 °C under residual pressure.[41]

The physical properties of the $Zn_{1-x}Fe_xO$ films are directly related to the nature of the phases present as a function of the x value.

$0 < x < 0.35$: optically transparent films are grown with the ZnO like-structure. However, the resistivity drastically increases with the increasing iron content, meaning that such films cannot be used for transparent conductive oxide applications. Moreover, noticeable magnetic properties have not been evidenced in this iron concentration domain, *i.e.* such Fe-doped ZnO films do not behave as diluted magnetic semiconductors.

$0.65 < x < 1$: the films crystallize in the spinel phase, and for growth under reducing conditions, they display remarkable ferromagnetic and spin polarized charge transport properties, which have been described in detail in a previous report,[13] and could lead to interesting applications in spintronics.

In the intermediate region where the wurtzite and spinel phases coexist, the physical properties of the nanocomposite films depend upon the respective fraction of the transparent highly resistive wurtzite phase and of the half metallic ferromagnetic zinc ferrite spinel phase. For increasing x values, both the resistivity and optical transparency decrease. For $x = 0.65$ such nanocomposite films present both a noticeable reduced optical transparency (<60%) in the visible wavelength domain with respect to the wurtzite-type films and a reasonably low resistivity (5×10^{-2} Ω cm), the two properties searched for in view of photoelectrochemical water splitting. As a matter of fact, it has been recently shown that Fe_3O_4–ZnO nanoparticles on graphene could be promising candidates for solar hydrogen production.[42] Besides, the existence of two distinct oxide nanocrystalline phases in thin films could induce a low thermal conductivity *via* the phonon scattering at the interfacial boundaries between the two phases, which coupled with the reasonable electrical conductivity may open the way for good thermoelectric properties.[43]

Conclusion

The phase diagram of $Zn_{1-x}Fe_xO$ films grown by PLD under reducing conditions on sapphire substrates has been investigated in the whole $0 < x < 1$ range, *i.e.* from ZnO to Fe_3O_4. Three domains have been clearly identified. For $0 < x < 0.3$, the films adopt the ZnO-like structure without noticeable electrical or magnetic properties, except for the fact that the Fe incorporation is accompanied by a very steep increase of the resistivity. For $0.35 \leq x \leq 0.65$, the existence of two distinct crystalline phases (ZnO-like and Fe_3O_4-like) induces reasonable optical absorption in the visible wavelength domain while limiting the electrical conductivity. These nanocomposite films may be envisaged as photoanodes in water splitting or alternatively may open the way for thermoelectric applications. For $x > 0.65$, pure spinel $Zn_yFe_{3-y}O_4$ films are grown displaying room temperature ferromagnetism and spin polarized charge transport properties.

Acknowledgements

The RBS measurements were performed under the Convention for SAFIR@ALTAÏS between The Université Pierre et Marie Curie and The University of Namur. The authors wish to thank S. Hidki for her help in XRD experiments. E. M. and J. P. would like to thank C. Boulmer Leborgne and S. Johansson for enlightening discussions.

References

1 T. Dietl, H. Ohno, F. Matsukura, J. Cibert and D. Ferrand, *Science*, 2000, **287**, 1019.
2 Z. W. Jin, T. Fukumora, M. Kawasaki, K. Ando, H. Saito, T. Sekigushi, Y. Z. Yoo, M. Murakami, Y. Matsumoto, T. Hasegawa and H. Koinuma, *Appl. Phys. Lett.*, 2001, **78**, 3824.
3 C. Liu, F. Yun and H. Morkoc, *J. Mater. Sci.*, 2005, **16**, 555.
4 H. J. von Bardeleben, N. Jedrecy and J. L. Cantin, *Appl. Phys. Lett.*, 2008, **93**, 142505.
5 K. Potzger and S. Zhou, *Phys. Status Solidi B*, 2009, **246**, 1147.
6 S. Mal, S. Nori, C. Jin, J. Narayan, S. Nellutia, A. I. Smimov and J. T. Prater, *J. Appl. Phys.*, 2010, **108**, 073510.
7 D. Karmakar, S. K. Mandal, R. M. Kadam, P. L. Paulose, A. K. Rajarajan, T. K. Naith, A. K. Das, I. Dasgupta and G. P. Das, *Phys. Rev. B: Condens. Matter Mater. Phys.*, 2007, **75**, 144404.
8 H. Liu, J. Yang, Y. Zhang, B. He and F. Pan, *Mater. Chem. Phys.*, 2008, **112**, 1021.
9 I. Soumahoro, R. Moubah, G. Schmerber, S. Colis, M. A. Aouaj, M. Ait, M. Abd-Lefdil, N. Hassanain, A. Berrada and A. Dinia, *Thin Solid Films*, 2010, **518**, 4593.
10 S. Q. Zhou, K. Potzger, G. Talut, H. Reuther, J. von Borany, R. Grotzschel, W. Skopura, M. Helm, J. Fassbender, N. Volbers, M. Lorenz and T. Hermannsdorfer, *J. Appl. Phys.*, 2008, **103**, 023902.
11 E. Le Boulbar, E. Millon, J. Mathias, C. Boulmer-Leborgne, M. Nistor, F. Gherendi, N. Sbaï and J. B. Quoirin, *Appl. Surf. Sci.*, 2011, **257**, 5380.
12 J. Perrière, C. Hebert, N. Jedrecy, W. Seiler, O. Zanelatto, X. Portier, R. Perez-Casero, E. Millon and M. Nistor, *J. Appl. Phys.*, 2014, **116**, 123502.
13 N. Jedrecy, C. Hebert, J. Perrière, M. Nistor and E. Millon, *J. Appl. Phys.*, 2014, **116**, 213903.
14 J. Narayan, K. Dovodenko, A. K. Sharma and S. Oktyabrsky, *J. Appl. Phys.*, 1998, **84**, 2597–2601.
15 J. Narayan and B. C. Larson, *J. Appl. Phys.*, 2003, **93**, 278.
16 M. Nistor, J. Perrière, C. Hebert and W. Seiler, *J. Phys.: Condens. Matter*, 2010, **22**, 045006.
17 J. Perrière, C. Hebert, A. Petitmangin, X. Portier, W. Seiler and M. Nistor, *J. Appl. Phys.*, 2011, **109**, 123704.

 This journal is © The Royal Society of Chemistry 2015

Published on 28 September 2015. Downloaded by Michigan State University on 19/01/2016 19:39:28.

18 E. Millon, M. Nistor, C. Hebert, Y. Davila and J. Perrière, *J. Mater. Chem.*, 2012, **22**, 12179.
19 C. H. Bates, W. B. White and R. Roy, *J. Inorg. Nucl. Chem.*, 1966, **28**, 397.
20 S. K. Mandal, A. K. Das and T. K. Naith, *Appl. Phys. Lett.*, 2006, **89**, 114105.
21 S. G. Protasova, B. B. Straumal, A. A. Mazilkin, S. V. Stakhanova, P. B. Straumal and B. Baretzky, *J. Mater. Sci.*, 2014, **49**, 4490.
22 D. Ghica, M. Stefan, C. Ghica and G. E. Stan, *ACS Appl. Mater. Interfaces*, 2014, **6**, 14231.
23 J. A. McLeod, D. W. Boukhvalov, D. A. Zatsepin, R. J. Green, B. Leedahl, L. Cui, E. Z. Kurmaev, I. S. Zhidkov, L. D. Finkelstein, N. V. Gavrilov, S. O. Cholakh and A. Moewes, *J. Phys. Chem. C*, 2014, **118**, 5336.
24 J. Takaobushi, H. Tanaka, T. Kawai, S. Ueda, J. J. Kim, M. Kobata, E. Ikenaga, M. Yabashi, K. Kobayashi, Y. Nishino, D. Miwa, K. Tamasaku and T. Ishikawa, *Appl. Phys. Lett.*, 2006, **89**, 242507.
25 A. P. Roth, J. B. Webb and D. F. Williams, *Solid State Commun.*, 1981, **39**, 1269.
26 M. Snure and A. Tiwari, *J. Appl. Phys.*, 2009, **106**, 043904.
27 P. A. Lee and T. V. Ramakrishnan, *Rev. Mod. Phys.*, 1985, **57**, 287.
28 M. Nistor, N. Mandache, J. Perrière, C. Hebert, F. Gherendi and W. Seiler, *Thin Solid Films*, 2011, **519**, 3959.
29 A. K. Das, R. S. Ajimsha and L. M. Kukreja, *Appl. Phys. Lett.*, 2014, **104**, 042112.
30 N. F. Mott, *J. Non-Cryst. Solids*, 1968, **1**, 1.
31 A. L. Efros and B. I. Shklovskii, *J. Phys. C*, 1975, **8**, L49.
32 K. Makise, K. Hidaka, S. Ezaki, T. Asano, B. Shinozaki, S. Tomai, K. Yano and H. Nakamura, *J. Appl. Phys.*, 2014, **116**, 153703.
33 Y. L. Huang, S. P. Chiu, Z. X. Zhu, Z. Q. Li and J. J. Lin, *J. Appl. Phys.*, 2010, **107**, 063715.
34 J. Tauc, R. Grigorovici and A. Vancu, *Phys. Status Solidi*, 1966, **15**, 627.
35 M. Sultan and R. Singh, *J. Appl. Phys.*, 2009, **105**, 07A512.
36 Z. B. Wu, M. Okuya and S. Kaneko, *Thin Solid Films*, 2001, **385**, 109.
37 D. Gao, Z. Shi, Y. Xu, J. Zhang, G. Yang, J. Zhang, X. Wang and D. Xue, *Nanoscale Res. Lett.*, 2010, **5**, 1289.
38 S. B. Ogale, *Adv. Mater.*, 2010, **22**, 3125.
39 Y. Hanzawa, D. Hiroishi, C. Matsuura and K. Ishigure, *J. Nucl. Mater.*, 1998, **252**, 209.
40 S. Zhou, K. Potzger, G. Talut, H. Reuther, K. Kuepper, J. Grenzer, Q. Xu, A. Mücklich, M. Helm, J. Fassbender and E. Arenholz, *J. Phys. D: Appl. Phys.*, 2008, **41**, 105011.
41 M. Hamieh, N. Jedrecy, C. Hebert, D. Demaille and J. Perrière, *Phys. Rev. B*, 2015, **92**, 155302.
42 N. Ysoff, S. V. Kumar, A. Pandikumar, N. M. Huang, A. R. Marlinda and M. N. An'amt, *Ceram. Int.*, 2015, **41**, 5117.
43 S. Valia, S. Balendhran, H. Nili, S. Zhuiykov, G. Rosengarten, Q. H. Wang, M. Bhaskaran, S. Sriram, M. S. Strano and K. Kalendar-zadeh, *Prog. Mater. Sci.*, 2013, **58**, 1443.